

Chapter 16

Residual Stresses in Cold Spray Coatings

Vladimir Luzin, Kevin Spencer, Mingxing Zhang, Neil Matthews,
Joel Davis, and Michael Saleh

16.1 Introduction

16.1.1 Stress in Cold-Sprayed Coatings

Cold spray is a relatively novel and rapidly developing technology for material deposition. In contrast to thermal spray technologies that deposit molten materials, it is believed that metallurgical bonding in cold spray is achieved in the solid state through the impact of feedstock material particles, accelerated to high speeds, 500–1000 m/s (Papyrin et al. 2007), towards a substrate, and with an accompanying large plastic deformation on impact. The link between spray conditions and coating properties is not fully elucidated. This is partly due to the complexity of the cold spray process, which involves different physical phenomena occurring at different structural scales. High strain rate deformation of the particles (up to 10^9 s⁻¹), and the resultant plastic shock wave, leads to the formation of micro-scale features such as adiabatic shear instabilities (~ 1 μm) and to the formation of ultrafine grains (~ 100 nm). On the mesoscale (10–100 μm), specific features are associated with splat morphology, voids, defects, inter-splat boundaries, etc. When the coating is formed, typically 0.5–5 mm thickness, gradients of stress and mechanical properties are observed through the whole thickness of the macroscopic scale.

V. Luzin (✉) • J. Davis • M. Saleh
Australian Nuclear Science and Technology Organisation,
Lucas Heights, NSW 2234, Australia
e-mail: vladimir.luzin@ansto.gov.au; joel.davis@ansto.gov.au; Michael.saleh@ansto.gov.au

K. Spencer • M. Zhang
School of Mechanical and Mining Engineering, The University of Queensland, St Lucia,
QLD 4072, Australia
e-mail: krs Spencer@gmail.com; mingxing.zhang@uq.edu.au

N. Matthews
Rosebank Engineering Pty Ltd, 836 Mountain Highway, Bayswater, VIC 3153, Australia
e-mail: neil.matthews@rosebank-eng.com.au

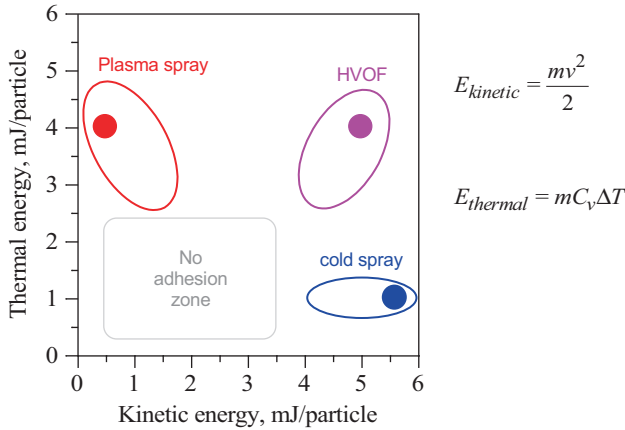


Fig. 16.1 Kinetic energy vs. thermal energy diagram for the three spraying techniques calculated for a 20- μm -size aluminium particle and typical spraying conditions

Cold spray is a highly energetic process as outlined in Fig. 16.1, and the deposited material undergoes some severe processes through microstructural modifications and transformations. These are driven by the large plastic deformations and the elevated temperatures experienced by the deposited particles. The deposition process almost always results into significant residual stresses.

The residual stress in coatings manufactured by the cold spray, which is usually compressive mostly due to kinetic impact of sprayed particles, is often considered from a structural integrity point of view since many physical properties, such as fatigue life or wear resistance, are intrinsically linked to the residual stress state. Therefore, the residual stress analysis became an important part of structural integrity assessment, especially when undesirable stresses (usually large tensile stress) are to be mitigated or, more commonly, when the spraying process is to be optimized to exploit the beneficial features of the residual stresses (usually moderate compressive stress). As such, it is imperative to consider residual stress as a factor in the overall mechanical performance and lifetime assessment of cold-sprayed samples or parts produced by cold spray. The residual stresses, resultant from the cold spray, exhibit interdependency on many spraying parameters, e.g. composition, temperature, particle velocity and particle size. The technological challenge is to tailor the residual stress together with other properties accordingly to the intended application through variations of the spraying parameters and deposition conditions.

However, apart from the technological and functional importance, experimental evaluation of residual stresses in coated systems can answer some deeper scientific questions. Since residual stress formation is intimately linked to the fundamental mechanisms of the cold spray deposition process, the deposition mechanisms can be studied through stress analysis, together with and in relation to other properties.

Despite some contemporary attempts to use cold spray (or thermal spray) to produce 3D objects in the manner of additive manufacturing techniques, the majority of spraying is done on very simple geometry – planar deposits and flat coatings.

Since technological coating thicknesses range from 0.1 mm (e.g. thermal barrier coatings or WC coatings) to several millimetres for surface restoration applications, the experimental technique used to study residual stresses usually require high spatial resolution.

16.1.2 Techniques for Stress Measurements in Coatings

In order to characterize the stress distribution in coating-substrate systems and to resolve the stress in the through-thickness direction, several traditional stress measurement techniques have been used. Methods such as residual curvature measurement for thin films were first carried out by Stoney (1909). Subsequent studies have utilized in situ curvature measurement on thick coatings (Matejcek and Sampath 2003), hole drilling techniques (Santana et al. 2008), X-ray diffraction combined with layer removal method (Santana et al. 2008) and synchrotron radiation (Genzel 2004) to measure stress in coatings or under the treated surfaces.

The general principles used in neutron diffraction stress measurements are well established, and the readers are referred to the works of Hutchings and Krawitz (1992) and Hutchings et al. (2005) for a more comprehensive review of the technique. The applicability of this technique and its suitability to the analysis of coatings, as well as to other many components, rely on the high penetration of neutrons. The half-attenuation depth of neutrons is ~6 mm in steel, ~60 mm in copper and ~60 mm in aluminium, while for X-rays, this value is ~100 μm at best. This high penetration depth of neutrons allows for through-thickness stress scanning in coated samples in totally non-destructive manner. Unlike X-ray-based methods, neutrons are very insensitive to sample surface finishes and do not require any special sample preparations.

Despite successes in the use of neutron diffraction techniques at the turn of the century (Matejcek et al. 1997; Matejcek et al. 1999), the use of neutron diffraction in last two decades has been restrained with respect to analysis of cold or thermally sprayed coatings. This has mostly been due to instrumental limitations: medium spatial resolution (gauge volume size) of ~1 mm, which still poses an issue on some neutron stress scanners, somewhat restricted access to neutron facilities and possibly the lengthy measurement times required for reliable statistics to be gathered. The latter point has consequently led to severe limitations on sample throughput, a key point in optimizing varying coating-substrate configurations. Historically the medium (limited to ~1 mm) spatial resolution led to the so-called partial illumination effect, an experimental artefact resulting from the uneven scattering density within a gauge volume. This usually takes place in near-surface regions and requires analytical or experimental mitigation (Pirling 2011; Suzuki et al. 2013).

However, with the new generation of specialized neutron residual stress diffractometers, which operate at constant wavelengths, such as SALSA (ILL, France), STRESS-SPEC (TUM, Germany) and KOWARI (ANSTO, Australia), stress measurements with high spatial resolution have become more readily available. The

neutron fluxes of these instruments allow a reduction in the spatial resolution, down from 1.0 to 0.1–0.2 mm (Luzin et al. 2017), while maintaining a practical measurement time, usually 5–30 min per point depending on material, sample dimensions, accuracy requirements, etc. With the higher spatial resolutions, the partial illumination problem is conveniently and effectively negated if the gauge volume remains at least 0.1–0.2 mm away from the surface/interface. The short measurement time allows for multiple samples to be studied efficiently, usually six to ten samples within a few days of a typical neutron experimental beam time allocation. The experimental uncertainties associated with neutron stress measurements can be as small as 5 MPa, though actual uncertainties are strongly dependent on elemental composition of the coating-substrate material and on the volume fraction, when investigating multiphase coatings.

In considering the advantages and benefits of the neutron diffraction technique, the acute shortage of suitable instruments around the world poses the most serious limitation on widespread adoption of the technique. The neutron diffraction scanners available for such experiments are largely confined to the very short list of facilities mentioned above. Moreover, time-of-flight instruments based on spallation sources, such as ISIS (UK), SNS (USA) and J-PARC (Japan), are not typically suited to high spatial resolution measurements due to their design constraints.

16.2 Analytical and Experimental Foundation of the Neutron Stress Measurements in Coatings

Coatings produced by cold spray, or by any other spraying technique for that matter, have certain experimental and analytical advantages when flat geometry is utilized, e.g. square coupons. Flat geometry allows for certain assumptions to be made and allows for more affective stress analysis of cold-sprayed samples based on the following considerations:

1. For flat sample geometry, the stress state can be simplified and can be described accurately using an assumption of zero plane stress state with the normal-to-surface stress component equal to zero ($\sigma_N = 0$). The zero plane stress condition is accurate on the outer surfaces, while it is still very accurately fulfilled through the interior regions in the through-thickness direction. Irrespective of the sample's composition, this assumption holds true with good accuracy for typical coating and substrates, in the order of several millimetres in thickness, under condition that the lateral dimensions are greater than the thickness dimension when the edge effects (stress relief on the outer edges) can be neglected. As a rule of thumb, for samples with a lateral dimension to thickness ratio of 10:1, the edge effects do not affect the uniform-in-plane stress state in the central part of the samples, where the plane stress condition is fulfilled with great accuracy.
2. Coating properties are usually uniform in the in-plane directions, assuming being away from edges; therefore, the stress state is fully characterized by the through-thickness distributions of the in-plane stress components, and the stress

can be treated as a one-dimensional function. Therefore, measurements can be done along one line through the sample's thickness greatly minimizing the amount of experimental work, in comparison with more 2D and 3D stress distribution fields that generally require 2D and 3D scanning.

3. The stress state in coatings is also usually equal-biaxial. This is valid in most cases as the process of coating deposition is usually transversely (in-plane) isotropic, assuming the particle stream impacts perpendicular to the surface. Thus, under this assumption only the in-plane stress component needs to be determined, and it fully describes the stress state. Experimentally, this reduces measurements to only two directions, one in-plane and one normal-to-surface (Fig. 16.2), though the equal biaxiality assumption can be experimentally checked by measuring the other in-plane direction, orthogonal to the first one. An example of such confirmational experiments is shown in Fig. 16.3. The three-directional experiment is essential if the assumed transversely isotropic symmetry is absent, e.g. the spraying direction is not perpendicular to the surface but under an oblique angle to the surface.
4. Another advantage is that d_0 -problem – finding a proper local stress-free d -spacing or d_0 – can be treated efficiently at once by measuring the d -spacing in two directions, in-plane d_{\parallel} and normal d_{\perp} , so that Hooke's equations (diffraction case) can be resolved for one in-plane stress component (henceforth referred to as stress) and the d_0 value are resolved concurrently as the two unknowns:

$$\sigma_{\parallel} = \frac{1}{\%aS_2} \frac{d_{\parallel} - d_{\perp}}{d_0} \quad \text{and} \quad d_0 = \frac{1}{\%aS_2} \{ (\%aS_2 + 2S_1) d_{\perp} - 2S_1 d_{\parallel} \} \quad (16.1)$$

where $S_1 = S_1(hkl)$ and $\frac{1}{2}S_2 = \frac{1}{2}S_2(hkl)$ are the diffraction elastic constants of the chosen diffraction reflection (hkl) .

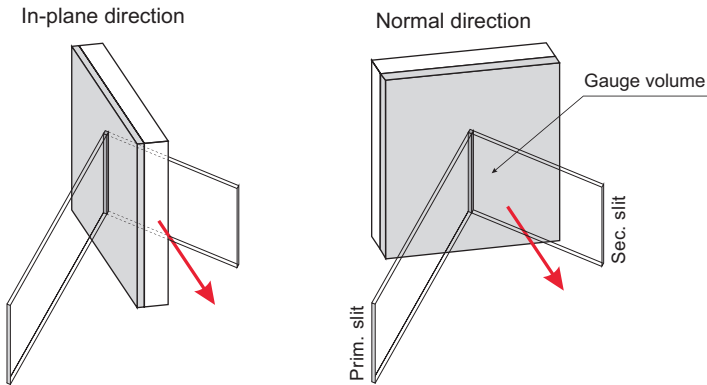


Fig. 16.2 Scattering geometry with two sample orientations for measurements of the two principal directions. The gauge volume is formed by intersection of the incident neutron beam coming through the primary slit and going out through the secondary slit

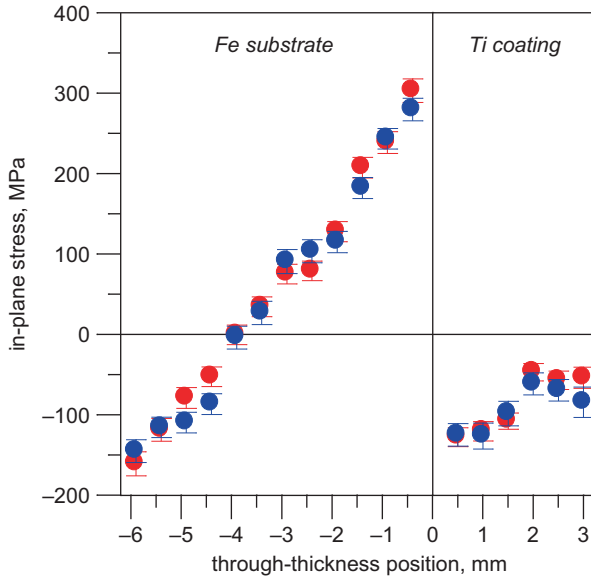


Fig. 16.3 Examples of residual stress equal biaxiality check for a cold-sprayed Ti/Fe sample when two orthogonal stress components (*red* and *blue*) were determined independently. The stress state is biaxial within experimental uncertainties

5. Another notable theoretical consideration relates to the treatment of the in-plane stress component. There is no theoretical framework that necessitates the in-plane stress to be a continuous function across the substrate-coating interface. Conversely, for the normal stress component, these continuity requirements are well explicated, but since these equate to a zero stress component, it is a trivial result. Therefore, through-thickness stress profiles in substrate-coating systems can and usually do exhibit a marked discontinuity at the interface. This is evident in all the experimental and the theoretical profiles reported below.
6. Some favourable experimental implications arise from the simplicity of the considered flat geometry and the simple stress state. In this case the experimental gauge volume can be extended in the in-plane direction (practically to 20–25 mm in the in-plane dimension); thus, even with a small slit size of 0.2 mm, the overall gauge volume remains considerable, 1 mm³ (0.2 × 0.2 × 25 mm³); see also Fig. 16.2 for illustration. This allows for rapid stress measurements (by neutron standards) with typical measurement time of ~10 min. As discussed above, 0.1–0.2 mm spatial resolution is congruent to most typical practical applications with the ability to resolve the stress distribution within a few millimetres.
7. From the experimental point of view, using a smaller gauge volume size of ~0.2 mm in the through-thickness direction can essentially eliminate the necessity of dealing with the partial illumination problems. This allows to maintain a fully immersed gauge volume, while still being close enough to the surface/interface. Therefore, measurements with no partial illumination interference can be made as close to the surface as 0.1–0.2 mm. The 180°-flip

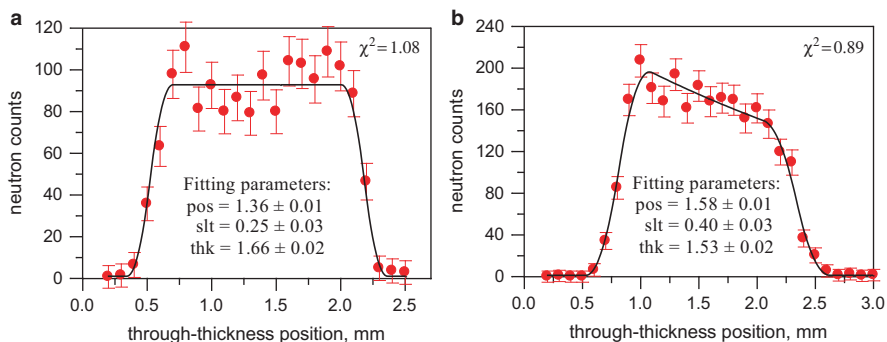


Fig. 16.4 Examples of the integrated intensity profiles obtained in the transmission (**a**, *left*) and reflection (**b**, *right*) geometries by scanning through plate of 1.6 mm thickness (thk) using 0.2 mm slits (slt). Profile fitting (*black lines*) results in the positioning (pos) accuracy of 0.01 mm. Experimental (nominal) gauge volume was $0.2 \times 0.2 \times 16 \text{ mm}^3$

strategy, which is sometimes used to deal with partial illumination experimentally, might still be useful in addressing similar experimental effects related to gradients of texture or composition; non-uniformity of scatterer; porosity in the sample; and the presence of unknown internal defects, voids and boundaries.

8. High spatial resolution, 0.1–0.2 mm, however, dictates higher positioning accuracy requirements, especially for the shallowest points that can suffer from some partial illumination effects. Ideally, this accuracy should be 0.01–0.02 mm (or ~10% from the spatial resolution) to eliminate such possibility. This accuracy is practically achievable through the use of the surface intensity scans that can resolve such positional accuracy, provided there are no complications arising from large grain sizes, presence of texture gradients or large defects. The use of mechanical, optical or laser scanning positioning systems cannot easily guarantee the required accuracy. A typical example is given in Fig. 16.4 to demonstrate the intensity scan procedure.
9. In order to achieve high spatial resolution experimentally, slits/apertures made of highly neutron-absorbing materials (Cd, Gd, B) are usually used. They are employed as the neutron optical systems of choice, since the neutron radial collimators, an alternative to slits, cannot provide any practical solution for gauge volume sizes less than 0.5 mm. Measurements with slits do not exhibit any disadvantages in comparison with the radial collimators, such as neutron beam divergence, in case of coatings. A high spatial resolution experiment usually assumes a small sample thickness of 1–5 mm. This also conveniently allows small slit-to-sample distances of the same order, therefore minimizing the neutron beam divergence. Theoretically, the divergence takes place, and it can result in a larger gauge size when compared with the nominal gauge size, but this effect is rather small: for a typical 5 mm slit-to-sample distance, the gauge volume size enlargement is ~0.01 mm for the primary beam and ~0.02 mm for the secondary beam (as in case of KOWARI, see below).

10. Since stress distribution in coatings is a one-dimensional elasticity problem, it can be easily interpreted and modelled without the use of finite element models (FEM), which are usually required for general three-dimensional elasticity problems. The layer deposition model developed by Tsui and Clyne (1997a) allows for an empirical description of the one-dimensional stress distribution in the coating-substrate system. The model has only two fitting parameters: one is the deposition stress σ_d , which is characteristic of the spray process and can be tensile (quenching) or compressive (peening). The deposition stress is obviously controlled by the deposition process' physical parameters (particle temperature and velocity) and the particle's material properties. The second parameter is the thermal mismatch $\Delta\epsilon_{th}$ that accounts for the discrepancy in the thermal expansion coefficient between the substrate and coating materials, $\Delta\epsilon_{th} = \Delta\alpha\Delta T$, when the temperature of the coating-substrate system drops by ΔT at the end spraying process. Quantitative analysis of the experimental stress profiles in terms of the model allows separation of σ_d and $\Delta\epsilon_{th}$ and their contribution into the final stress state. Further simplifying the main idea of the analysis, these two terms can be separated through the accurate measurement of the two slopes in the stress profiles across coating and substrate.

The model was successfully applied to a range of deposition techniques such as plasma spray, high-velocity oxygen-fuel (HVOF) and cold spray (Fig. 16.5). The stress profiles in Fig. 16.5 show the deposition stress parameter that extracted experimentally, while the thermal mismatch stress is essentially zero as there are no discernible differences in the thermal expansion coefficient in the Al/Al systems. It should be noted that for the cold-sprayed samples, the deposition stress is compressive, -22 MPa. Conversely for the plasma spray sample, the deposition stress is tensile, $+10$ MPa, while for the HVOF sample, the value lies between these two. This observation is a manifestation of the dominant stress-inducing mechanism of the three techniques: peening in the cold spray, quenching in the plasma spray and combination of both in the HVOF. While the layer deposition model deals with the case of free-standing substrate, which is allowed to bend and deform during the deposition process, often other constrained conditions are also considered in accordance with the sample fixation method (Brenner and Senderoff 1949).

11. Analysis of the experimental stress profile in terms of the deposition stress and thermal mismatch, and its decomposition into the two contributions, is essential for the interpretation of the measured stress profiles and, specifically, for the purpose of comparing stresses from different coatings. The resultant stress profiles encompass not only the deposition process parameters, σ_d and $\Delta\epsilon_{th}$, but also the dependences on coating and substrate thicknesses and material properties. In Fig. 16.6a several simulated stress profiles are shown to illustrate changes as a function of the coating's thickness. While the profiles exhibit measurable differences due to thickness variation, when these profiles are back calculated in terms of deposition stress, all profiles will result in the same deposition stress parameters σ_d (and $\Delta\epsilon_{th}$ for that matter). The same effect can be observed for changes in substrate material (elastic properties) as shown in Fig. 16.6b.

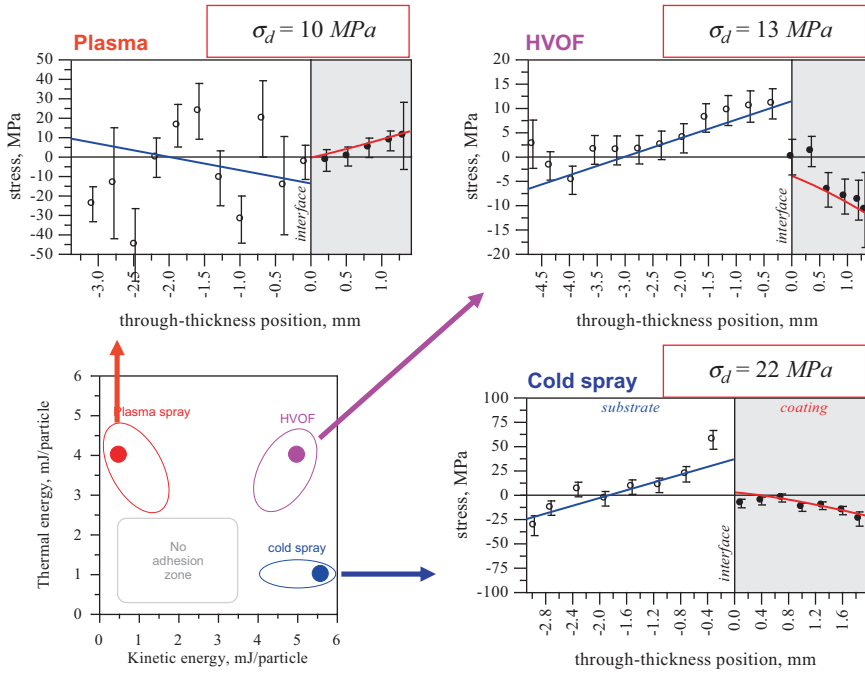


Fig. 16.5 Results of the stress analysis using Tsui and Clyne model for Al/Al-coated samples (substrates are at the *left*, coatings are at the *right*) sprayed by three different techniques. Details can be found in Luzin et al. (2008) (experimental data in the substrate of “plasma” sample is unreliable due to grain size problem resulting in huge statistical oscillations)

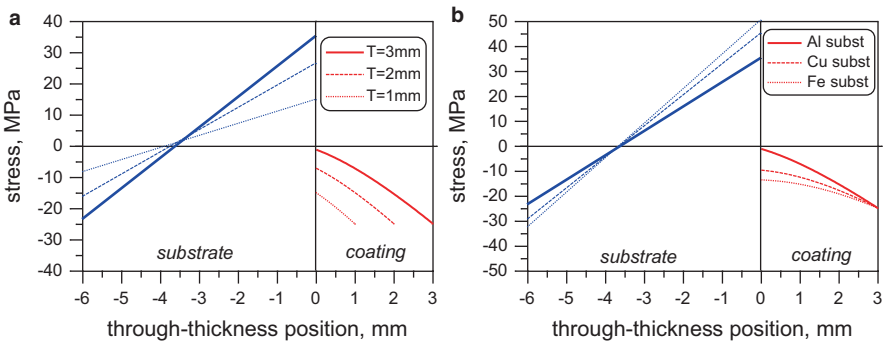


Fig. 16.6 (a, *left*) Three stress distributions resulting from the same deposition stress (-25 MPa) but for three different coating thicknesses (3, 2 and 1 mm). (b, *right*) Three stress distributions calculated with the same thickness (3 mm), the same deposition stress (-25 MPa) but different substrate material (*Al*, *Cu* and *Fe*). Coating material is *Al* with Young’s modulus of 47 GPa . There is no thermal mismatch term for simplicity

Therefore by performing the above analysis and separating the different contributions, all geometrical factors are eliminated. While the thicknesses of coatings might differ or substrate properties may change, this analysis provides a reliable tool to compare stress in various coatings. Moreover, it can be used for prediction or recalculation of stress profiles in systems of various combinations.

12. The layer deposition model only predicts stresses occurring during the deposition of the coating atop the substrate. However, the experimental stress distributions might display some pre-spraying (initial) stresses, which can exist in the substrates, in addition to the stresses induced by the spraying process. These residual stresses in substrates are usually inherited from the production processes, e.g. rolling, quenching or pre-spraying substrate preparation, e.g. grit/sand blasting. Several strategies are used to address this issue: (i) substrates can be stress relieved prior to coating through annealing. This strategy may not always be available or appropriate for certain cases, e.g. annealing samples after grit blasting might not be deemed acceptable due to the potential for surface oxidation. (ii) A more practical way is to measure stress distribution in the substrates directly and subsequently subtract it from the coated sample profile. The resultant stress distribution can then be treated within the frame of the layer deposition model. This is illustrated in Fig. 16.7a based on the data from the cold-sprayed Al/Al sample (Choi et al. 2007). The expected stress profile in the substrate is a linear function since the substrate can experience only bending, assuming that no material modification occurs during coating. (iii) Alternatively, the initial stress can be an integral part of the extended modelling. This approach is also illustrated in Fig. 16.7b for the same Al/Al system. However, this approach is only practicable in a few simple cases such as peening stress or plastic bending stress, as these are relatively simple and can be easily parametrized with a few empirical constants. In the case of Fig. 16.7b, the peening stress is described by the width and intensity parameters of an eigenstrain function (Korsunsky 2005).
13. For experimental resolution of 0.2 mm, the stress profiling is practical for relatively thick coatings of few millimetres down to 0.4–0.5 mm (Luzin et al. 2017). However, there is a clear limit for this approach. When the coating thickness is reduced and becomes commensurate with the finest attainable resolution of 0.2 mm, the stress profiling through the coating is no longer practically possible. At the best, only the average through-thickness stress value can be obtained experimentally. In this case the stress decomposition cannot be done unambiguously as illustrated by Fig. 16.8.

The two simulated stress profiles have identical stress distributions in the substrate, identical average through-thickness stresses, but they are representative of two different mechanisms of stress generation. In Fig. 16.8a the stress is attributed to the thermal mismatch (with a deposition stress equal to zero), while for the second case, Fig. 16.8b, the profile is fully determined by the deposition stress (with a thermal mismatch equal to zero). This ambiguity can be resolved by fixing one of the parameters, usually the thermal mismatch term, as it can be conveniently measured using thermocouples in laboratory conditions.

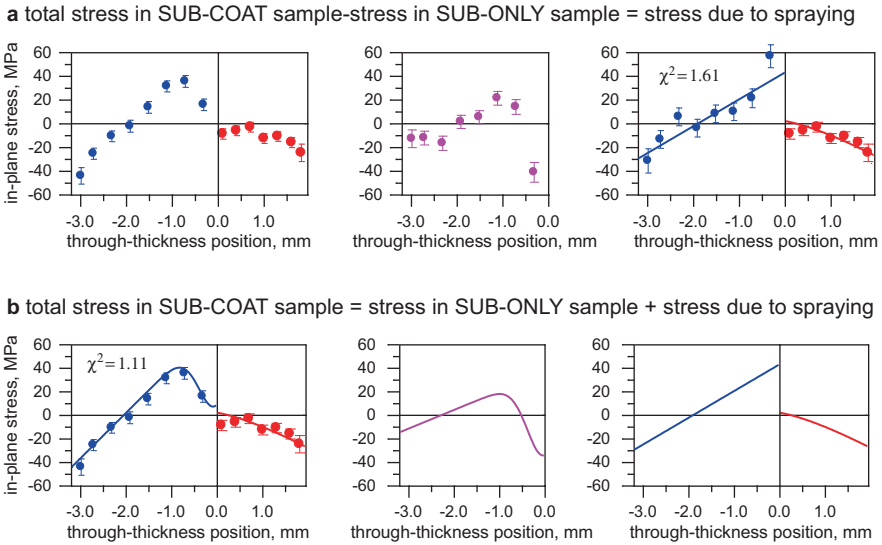


Fig. 16.7 Two ways of dealing with an initial stress distribution in substrate through (a, top) subtraction of the experimental profile and fitting the result or (b, bottom) fitting the as-measured profile with inclusion of the initial stress as a part of the model description

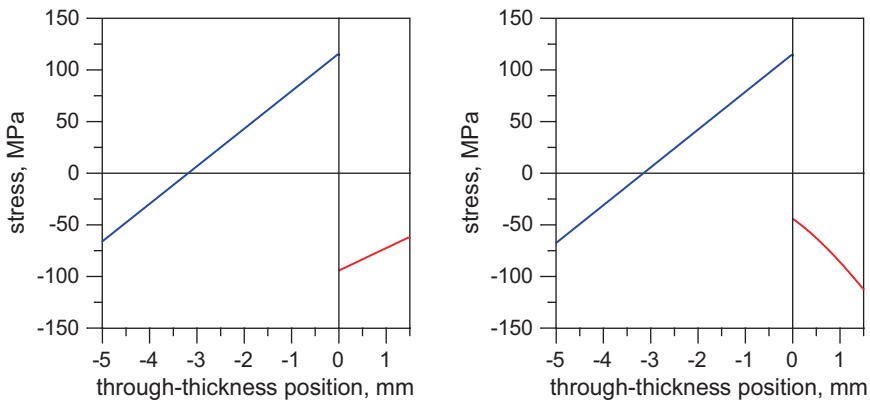


Fig. 16.8 Two stress distributions which correspond to two different mechanisms, thermal mismatch (a, left) and peening (b, right), correspondingly

14. Although only single-phase coatings are considered in the manuscript, there is an opportunity with neutron stress scanning to measure two-phase (multiphase) materials in a similar way. The measurement protocol involves measuring each phase separately and the separation of the micro- and macro-stress as described by (Luzin et al. 2010).

15. Although the study of the spray and deposition processes on flat coated samples (flat geometry) may seem like an oversimplification, considering the complex shapes of various industrial components, there are ways to transfer these stress characterizations to more complex geometries. One way is through an analytical approach where the stress parametrization through deposition/thermal mismatch can be applied to other geometries; an example of cylindrical geometries is shown in Tsui and Clyne (1997b). Another way is to use the same parametrization in combination with FEM modelling to compute the local stress at a scale at which sample is locally flat.

16.3 Experimental

In this work we present a systematic study of different materials sprayed using different conditions and cold spray techniques for flat coating geometries. They were studied using neutron residual stress measurement technique as well as several other analytical techniques, to accompany the residual stress analysis. The aim of the study is to establish fundamental understanding of the residual stress formations and also to provide insights on the mechanism of cold spray coating formation in general.

16.3.1 Samples and Spraying Procedures

In this study only pure metals were selected in three groups, FCC, BCC and HCP metals. A rather limited list of materials was composed, based on their availability, industrial relevance, safety issues and suitability to neutron experiment, with four representatives of FCC metals (Al, Cu, Ni, γ -Fe), three HCP metals (Ti, Zn, Co) and one BCC metal (α -Fe).

Samples for the study were sprayed using two cold spray systems:

- (i) A Kinetic Metallization (KM) system, manufactured by Inovati (USA) – a low pressure, sonic CS variant
- (ii) A CGT Kinetiks 4000, manufactured by Cold Gas Technologies (Germany) – a high pressure, supersonic CS variant

These two systems will be referred throughout the manuscript as KM and CGT.

Both systems operate under choked flow conditions. In the case of the KM system, the gas speed exiting the convergent barrel nozzle is \sim Mach 1, and the resultant gas speed depends on the gas used (He or N₂) and can be calculated using isentropic ideal gas relations at Mach 1 (Dykhuisen and Smith 1998). Higher (sonic) velocities can be reached by using He rather than N₂, because He gas has a lower molecular weight and higher specific heat ratio than N₂.

The CGT system uses a convergent-divergent nozzle and high gas driving pressure to produce supersonic conditions, a Mach number ~ 2 – 2.5 , at the nozzle exit. Even though only N_2 gas was used with this system, the exit particle and exit velocities were somewhat higher than the KM system using He gas, for the same particle size.

The data on gas temperature T and pressure P (immediately upstream of the nozzle throat) and the estimated exit particle V_p (Dykhuizen and Smith 1998) and gas exit velocity V_g are given in Table 16.1 for the KM process and Table 16.2 for CGT.

The Cu substrates were squares $30 \times 30 \text{ mm}^2$ in size and 2.6–2.8 mm thickness. They were cleaned with 1200 grit SiC paper and rinsed with ethanol immediately before spraying. Commercially pure spherical powders produced by gas atomization were used as the feedstock material. The powders used in spraying were as fine as possible to obtain dense coatings and had a particle size in the range 4–16 μm (Tables 16.1 and 16.2).

Coatings were sprayed to a typical thickness of 1–2 mm to provide enough material for characterization.

Table 16.1 KM processing parameters

| Sample | Size (μm) | Gas | P (MPa) | T ($^\circ\text{C}$) | V_g (m/s) | V_p (m/s) |
|--------|------------------------|-----|-----------|--------------------------|-------------|-------------|
| Al/Cu | 15 | He | 0.62 | 140 | 1035 | 585 |
| Cu/Cu | 6 | He | 0.62 | 200 | 1105 | 645 |
| Ni/Cu | 7 | He | 0.62 | 275 | 1195 | 630 |
| Zn/Cu | 8 | He | 0.62 | 65 | 935 | 535 |
| Ti/Cu | 16 | He | 0.62 | 365 | 1285 | 557 |
| Fe/Cu | 10 | He | 0.62 | 370 | 1295 | 580 |
| SS/Cu | 8 | He | 0.62 | 280 | 1200 | 625 |
| Co/Cu | 4 | He | 0.62 | 380 | 1305 | 870 |

Table 16.2 CGT processing parameters

| Sample | Size (μm) | Gas | P (MPa) | T ($^\circ\text{C}$) | V_g (m/s) |
|--------|------------------------|-------|-----------|--------------------------|-------------|
| Ti/Cu | 16 | N_2 | 3.9 | 615 | 640 |
| Fe/Cu | 10 | N_2 | 3.9 | 615 | 630 |
| SS/Cu | 8 | N_2 | 3.9 | 520 | 630 |
| Co/Cu | 4 | N_2 | 3.9 | 600 | 620 |

16.3.2 Coating Characterization Methods

1. The microstructure was characterized by employing scanning electron diffraction and EBSD to reveal microstructural features at the micro-scale level (e.g. small-angle boundaries and subgrain structure). The metallographic sections transverse to the spray direction were polished and chemically etched to reveal the particle boundaries. The analysis of average plastic strain of the particles in the coating was estimated by examining deformed particle shapes. It was assumed that on impact (i.e. uniaxial compression), the initially spherical particles were deformed into elliptical shapes (oblate spheroids in 3D). The analysis of aspect ratios $l_{\parallel}l_{\parallel}/l_{\perp}$ of multiple particles (~50 measurements for each sample) allowed for statistical evaluation of the average equivalent plastic strain,

$$\bar{\varepsilon} = \frac{2}{3} \ln(l_{\parallel} / l_{\perp}).$$

2. Coating density was measured using Archimedes method: rectangular bar specimens were cut from the coatings by electric discharge machining (EDM) with accuracy greater than ± 0.01 mm in the linear dimension. Since the bar thickness was the smallest dimension, the uniformity of the bar thickness was a critical parameter in the accuracy of the density determination. The density measured using this technique was estimated to be accurate to at least $\pm 1\%$ for the most thin specimens or better, down to 0.4%, when bar specimen thickness was several millimetres. Although only one specimen representative of the coating was used in the density evaluation procedure, in one case (Al, KM) several samples were tested to check reliability of the procedure with the results being in agreement within error bars.
3. The Young's modulus was determined using the impulse excitation technique (Heritage et al. 1988) on the same set of the rectangular bars sectioned from the coating. Yet again, the critical parameter determining the accuracy of the Young's modulus was through-thickness uniformity of the test specimens, and in a very similar way, the relative accuracy of the Young's modulus measurement was 1% at worst, while 0.5% was more typical.
4. Neutron diffraction texture analysis was carried out using the neutron diffractometer KOWARI (OPAL, ANSTO) (Kirstein et al. 2009). Several pole figures were measured on a $5^{\circ} \times 5^{\circ}$ grid to calculate the orientation distribution function. For FCC materials the set of the measured pole figures included (111), (200) and (220), while for the HCP material, the set was (002), (100), (101) and (110). The full pole figures were measured, despite cylindrical symmetry of pole figures, to provide better statistics when averaged over azimuthal angle. Samples for texture measurements were cuboids, with typical size of 5–6 mm, which allowed for a reduction in neutron absorption effects while retaining a sample volume that lends itself to improved neutron counting and grain statistics and, therefore, more reliable results.
5. The residual stress measurements were performed on the neutron diffractometer (stress scanner) KOWARI (Kirstein et al. 2009). A typical 0.2–0.5 mm gauge vol-

ume size was chosen in order to resolve the through-thickness stress distribution. To achieve the best possible through-thickness spatial resolution, the diffraction experiment was done in 90° geometry, and to achieve this, the wavelength of the instrument was varied according to the coating materials and the diffraction reflection used in the measurements. The typical wavelength was in the range of 1.5–1.8 Å; the reflection for FCC materials was (311), (211) for BCC and (112) for HCP. The neutron measurements were done through the whole thickness of the samples, both coating and substrate, to have full stress description of the coating-substrate elastic system. Since scattering properties of different materials vary significantly, the measurement time to measure one location (point) in the samples was also significantly different between samples. Adjustment of measurement time ensured strain measurement accuracy of $\sim 50 \mu$ strains.

Measurements were done accordingly to the protocol described in Sect. 16.2. At each through-thickness location, the diffraction peak position was measured along the two principle directions, in-plane and normal to calculate in-plane stresses assuming a state of balanced biaxial plane stress. In order to evaluate only stresses which originate from the cold spray process, the initially existing stresses in substrates were excluded by performing neutron stress measurements on the “substrate-only” sample and subtracting the obtained stress distribution out of the “coating-substrate” stress profiles.

6. Electron backscattering diffraction (EBSD) analysis was carried out on a transverse cross-section of a cold-sprayed Al6061 CGT coating sample, studied previously (Spencer et al. 2012). It was sprayed using $45 \mu\text{m}$ powder, N_2 as a carrier gas at a driving pressure of 3.9 MPa and a gas temperature 400°C . The EBSD map was post-processed using the HKL Channel 5 software. EBSD patterns were collected and analysed in an area $40 \times 30 \mu\text{m}^2$ around a triple-junction boundary of three particle splats, using a step size of $0.15 \mu\text{m}$.
7. Two complementary simulation approaches were used to study the cold spray process with high temporal (ns range) and spatial (μm range) resolution. The first method was a Lagrangian solid element (LE) method which has been successfully used in previous studies of particle impact (see, e.g. (Schmidt et al. 2009; Gu and Kamnis 2009; Grujicic et al. 2004)). This method allows for analysis of the first stage of the particle impact but often results in errors as the simulation progresses due to large element distortions and severe reduction of the computational time steps. The second method is the smooth particle hydrodynamic (SPH) formulation model realized in the hydrocode LS-DYNA. Because it is an element-free Lagrangian formulation, the singularity problem is effectively overcome, and the method allows modelling of the latter stages of deformation, as well as extending modelling to a multiparticle simulation. Simulations of the deposition process as well as the occurrence of debris or jetted particles and the peening stress were treated correctly in this formulation. In the current study, it was possible to simulate the deposition of 400 individual particles of Al6061 with particle size of $15 \mu\text{m}$, staggered in four layers, each comprising 10×10 particles. The particles impacted an Al6061 substrate surface at velocity of 585 m/s. The substrate dimensions were $200 \times 200 \times 60 \mu\text{m}$ and were also modelled using SPH elements, using a coarser resolution. A symmetrical SPH formulation (IFORM = 2) was used in

LS-DYNA, with a variable smoothing length option. The Johnson-Cook constitutive material model with a Mie-Grüneisen equation of state was used to describe the deviatoric and hydrostatic stress within the materials. All technical details of the modelling can be found in (Saleh et al. 2014b).

16.4 Results and Discussion

16.4.1 Coatings Microstructure

The microstructure of the sprayed coatings demonstrated good consolidated quality, with no significant bulk defects (Fig. 16.9). The microstructures of different samples were used to evaluate the average equivalent plastic strain that came for all material very close to -0.5 (see, e.g. a grain in the right bottom corner in Fig. 16.9 that lies at the interface).

16.4.2 Coating Densities

The apparent quality of the sprayed coatings observed using microscopy was confirmed by measuring the coating density, shown in Fig. 16.10. The coatings with a lower fractional bulk density were the BCC and HCP materials, which deform less readily than the FCC materials and likely have more boundary and bulk defects as a result. Another obvious observation is that the CGT consistently produces coatings

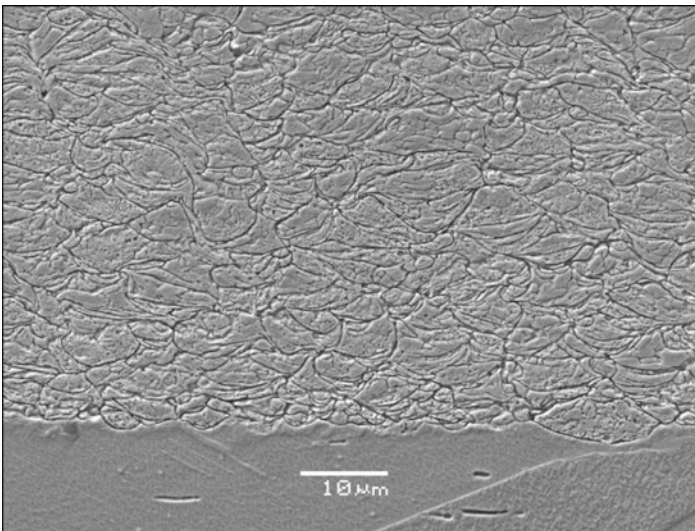


Fig. 16.9 Microstructure of the Cu coating produced by KM

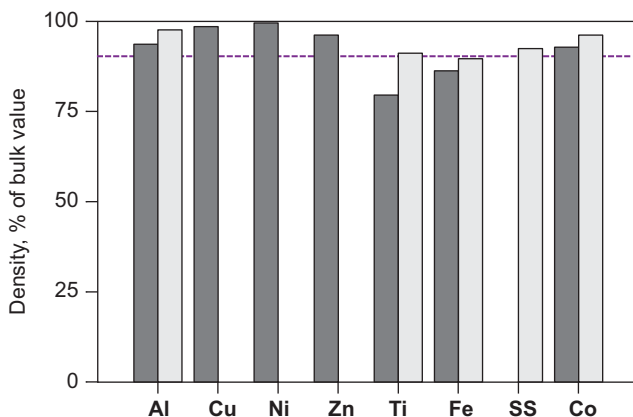


Fig. 16.10 The density of the coatings sprayed by KM (*dark*) and CGT (*light*), expressed as percentage of bulk density. Ninety percent level is marked by a *dotted line*

with a density closer to their bulk equivalents than the KM. The higher velocity in the CGT system and the higher resultant kinetic energy and impact pressure ensure better compaction of the coating materials. The initial deposition temperature may also play a role, but the extent of that influence is difficult to quantify at this stage and requires further study.

16.4.3 Coating Young's Modulus

While density is a measure of the volume porosity (3D defects), the Young's modulus is also sensitive to 2D defects such as cracks and the quality of the particle-particle interfaces. The latter has a stronger impact on the Young's modulus because the volume porosity alone would produce analogous reduction in both the densities and Young's modulus. The fact that Young's modulus can be as low as ~50% of the bulk value (Fe and Ni) or even less (in case of Ti) illustrates the importance of the interparticle bond quality (Fig. 16.11). As with density, the Young's modulus of CGT coatings is larger than for the KM coatings, and this effect is probably more distinct. This suggests that for CGT not only is the particle compaction better but so is the particle cohesion.

16.4.4 Texture Analysis

Examples of the experimental pole figures obtained in the neutron diffraction experiment are shown in Fig. 16.12. Although pole figures are supposed to have a cylindrical symmetry, due to statistical uncertainties, there are variations that are especially visible when textures are not very pronounced. Indeed, the resultant texture is

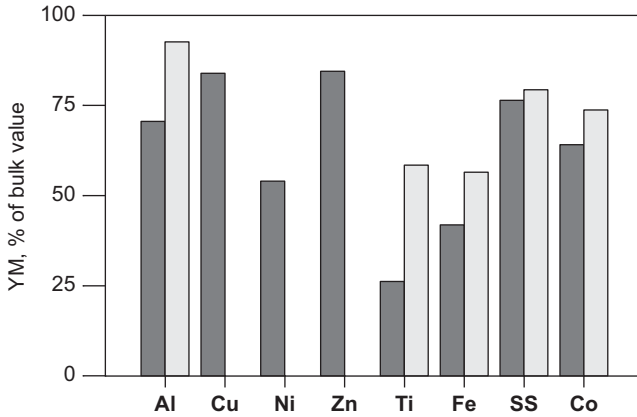


Fig. 16.11 The Young's modulus of the coatings sprayed by KM (*dark*) and CGT (*light*), expressed as percentage of bulk Young's modulus

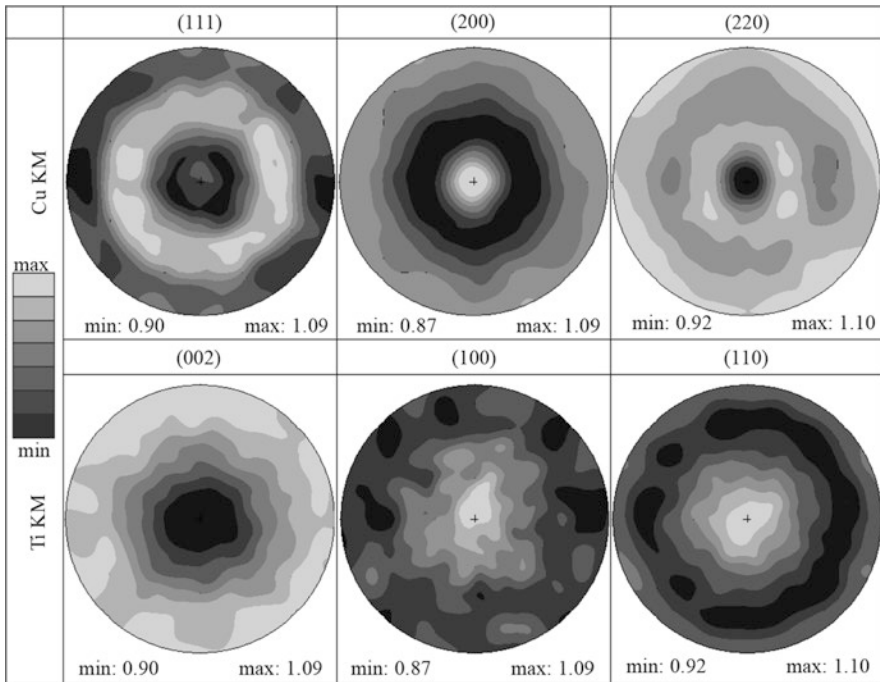


Fig. 16.12 Experimental pole figures for two samples (a) *Cu, KM* and (b) *Ti, KM* representing two kinds of materials, FCC and HCP (*dark colour* corresponds to maximum)

relatively weak. This is despite the fact that deformation of individual particles is large (~0.5 of equivalent plastic strain) and much stronger texture development is expected. In order to improve the statistics, the pole figure densities obtained by azimuth angle averaging of the measured full pole figures are shown in Fig. 16.13, as

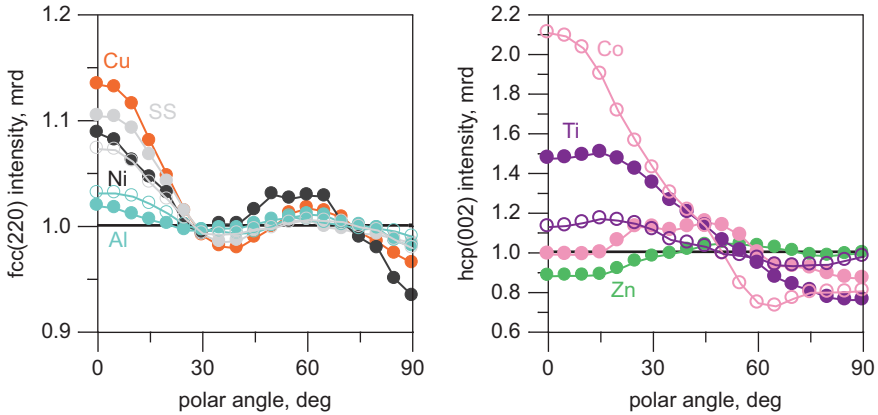


Fig. 16.13 Pole figure densities for different samples produced by KM (*solid symbols*) and CGT (*empty symbols*)

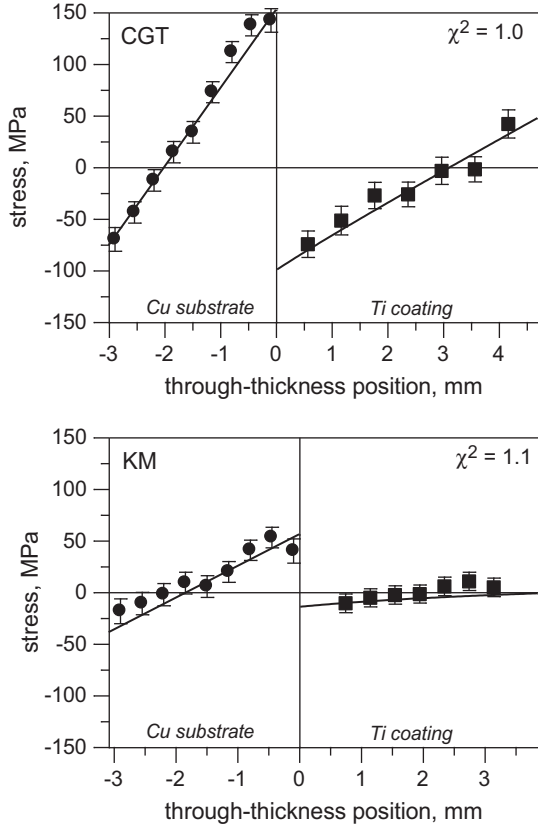
a function of the polar angle only. Pole figures demonstrating the largest min/max ratio were chosen to illustrate texture data, FCC(200) and HCP(002). Examining the fibre components (Matthies et al. 1987; Cho et al. 2004), in case of the Cu sample, the apparent (110) fibre component, which is characteristic of slip on the dominant $\{111\}\langle 110\rangle$ slip system, has in fact very high intensity (90–100%). However, the width of this component is very large (65° – 70°), resulting in a weak texture. In the case of the Ti and Co CGT-sprayed samples, basal slip on $\{001\}\langle 110\rangle$ causes the appearance of the (002) fibre component, while for other HCP materials, Zn using the KM technique and Co utilizing the CGT technique, the fibre texture component is of the (10.1) type. In the same way as for FCC metals, the fibre components are broad (width of $\sim 70^\circ$), producing a weak texture. The BCC iron samples, for both KM and CGT, do not exhibit any measurable preferred orientation.

16.4.5 Residual Stress Analysis

A typical through-thickness residual stress distribution is shown in Fig. 16.14 for two Ti samples. The accuracy was estimated to be ± 10 MPa. In some cases the uncertainties were larger, and in the worst case of Co, the accuracy was ± 60 MPa. This was due to the fact that Co has very poor neutron scattering properties: small coherent cross-section (weak diffraction signal), large incoherent cross-section (large background) and high absorption (neutron beam attenuation).

The residual stress profiles were fitted using (Tsui and Clyne 1997a) progressive coating deposition model as described in Sect. 16.2. The quality of the model fit is confirmed by the χ^2 values which were typically close to 1 (e.g. Fig. 16.14). The same routine was applied to all other coating systems presented herein, allowing for separation of all contributions to the overall stress distribution (initial stress, deposition stress, thermal mismatch stress).

Fig. 16.14 Through-thickness stress distribution in Ti samples sprayed by (a) KM and (b) CGT



Separation of the contributions allowed the dominant stress formation factor in a given coating-substrate system to be determined. Thus, in the case of the Ti coating shown in Fig. 16.14, the dominant stress factor is the thermal misfit due to the substantial difference in thermal expansion coefficient between Ti and Cu. Along with this statement is the fact that stresses are larger in the CGT sample: the CGT (gas) spraying temperature of 615 °C is much higher than it is in KM, 365 °C, and this generates larger thermal residual stress for the higher temperature process. The contribution from the peening stress is relatively small: when considered alone it can produce stress profiles with a maximum value of only 20 MPa in the Cu substrate close at the interface. Thus, for both Ti coatings, the accumulated residual stress is thermal in origin rather than kinetic (i.e. due to a peening process).

The most important result of the analysis is the values of the deposition stress σ_d for different materials. The deposition stresses for all studied materials and techniques are shown in Fig. 16.15. It is confirmed that cold spray produces compressive deposition stress due to peening observed in earlier works (Luzin et al. 2008; Luzin et al. 2011; Spencer et al. 2012). The magnitude of the peening stress varies clearly with the sprayed material. It is notable that the HCP materials (Zn, Ti, Co) and BCC materials (Fe) did not accumulate a large residual stress, while the FCC

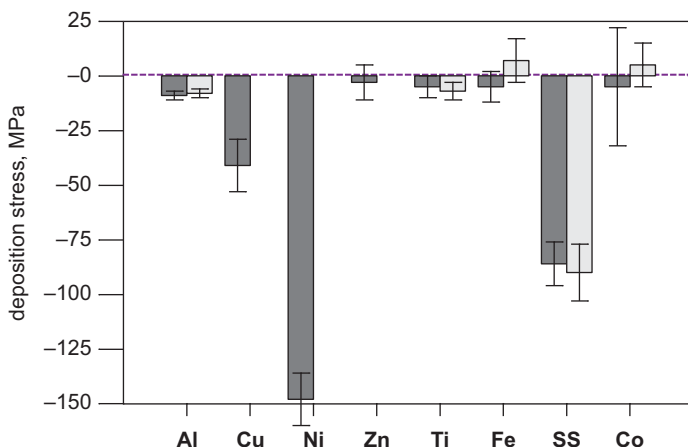


Fig. 16.15 The deposition stress for coatings sprayed by KM (*dark*) and CGT (*light*) techniques

materials (Al, Cu, Ni, stainless steel) tend to exhibit significantly higher level of residual stress. The stress in the FCC materials correlates with the yield stress (YS) of the sprayed material, though the corrections for the temperature dependence and rate dependence must also be considered. The same conclusion has been made based on analysis of cold-sprayed Al alloys (Spencer et al. 2012) and is illustrated in Fig. 16.16. Studying the Al/Al-coated systems eliminates other possibilities like dependence on thermal conductivity, density, Young's modulus, etc. since all elastic and thermal properties were essentially identical for all considered alloys.

16.4.6 EBSD Analyses

A secondary electron image of the EBSD scan region on the surface area of an Al6061 KM sample is shown in Fig. 16.17a, b. The EBSD analysis reveals a complex grain structure that can be visible in Fig. 16.17c. With the measurement resolution of $0.15 \mu\text{m}$, the estimated average subgrain size appears to be $\sim 0.5\text{--}1 \mu\text{m}$. Consistent with previous EBSD analysis done on a cold-sprayed Ni coating (Zou et al. 2009), there is evidence of an ultra-fined grain structure formed by dynamic recrystallization. The approach to estimate the mean grain size through the parameters of the deformation processes, outlined in (Twiss 1997) and used in (Zou et al. 2009) in the case of Ni, was also applied to the present Al6061 cold spray sample. Using an average impact pressure of $\sigma = 800 \text{ MPa}$ (Zou et al. 2009), Burgers vector $b = 0.286 \text{ nm}$ ($\frac{1}{2} \langle 110 \rangle$), aluminium shear modulus $G = 25.88 \text{ GPa}$ and constants $n = 0.8$ and $K = 15$ and the relationship between them, $(\sigma/G)(D_R/b)^n = K(\sigma/G)(D_R/b)^n = K$, the estimate of the grain size is $D_R \sim 0.7 \mu\text{m}$, close to the observed grain size. Away from the particle contact areas, the granular structure appears to be similar in size to the microstructure of the original particles (Fig. 16.17d).

Fig. 16.16 Correlation and proportionality between the deposition stress and YM of the aluminium alloys

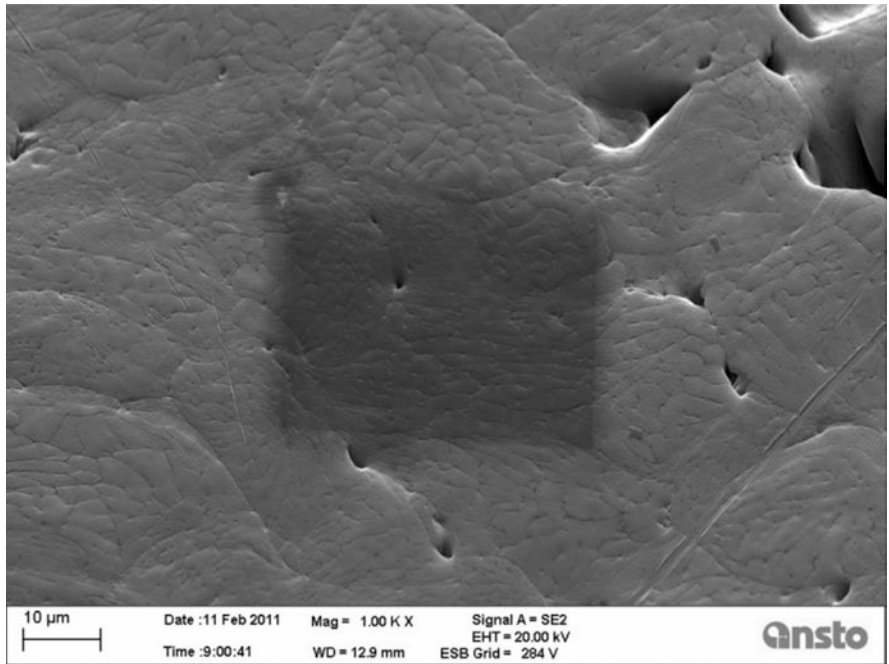
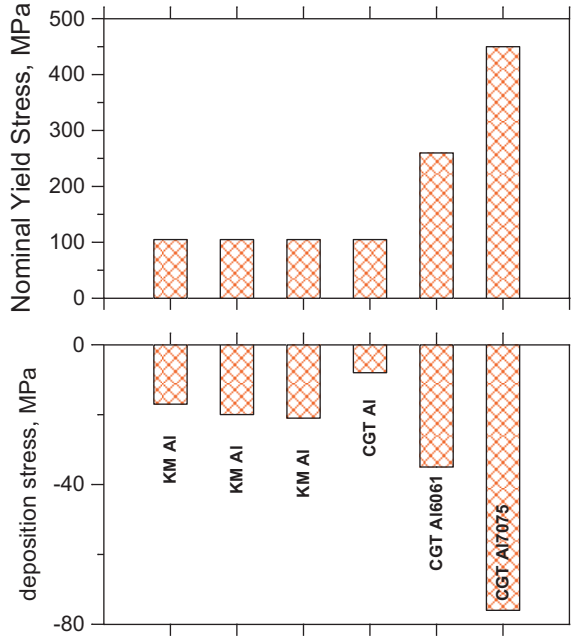


Fig. 16.17 (a) SEM image around the area that was analysed by EBSD and the central area, $40 \times 30 \mu\text{m}^2$, has a darker hue due to the exposure to the electron beam; (b) SEM image of the area that was analysed by EBSD and (c) EBSD map of this area plotted in Euler angle colour scheme and (d) comparison with the original grain structure of the powder particle before spray

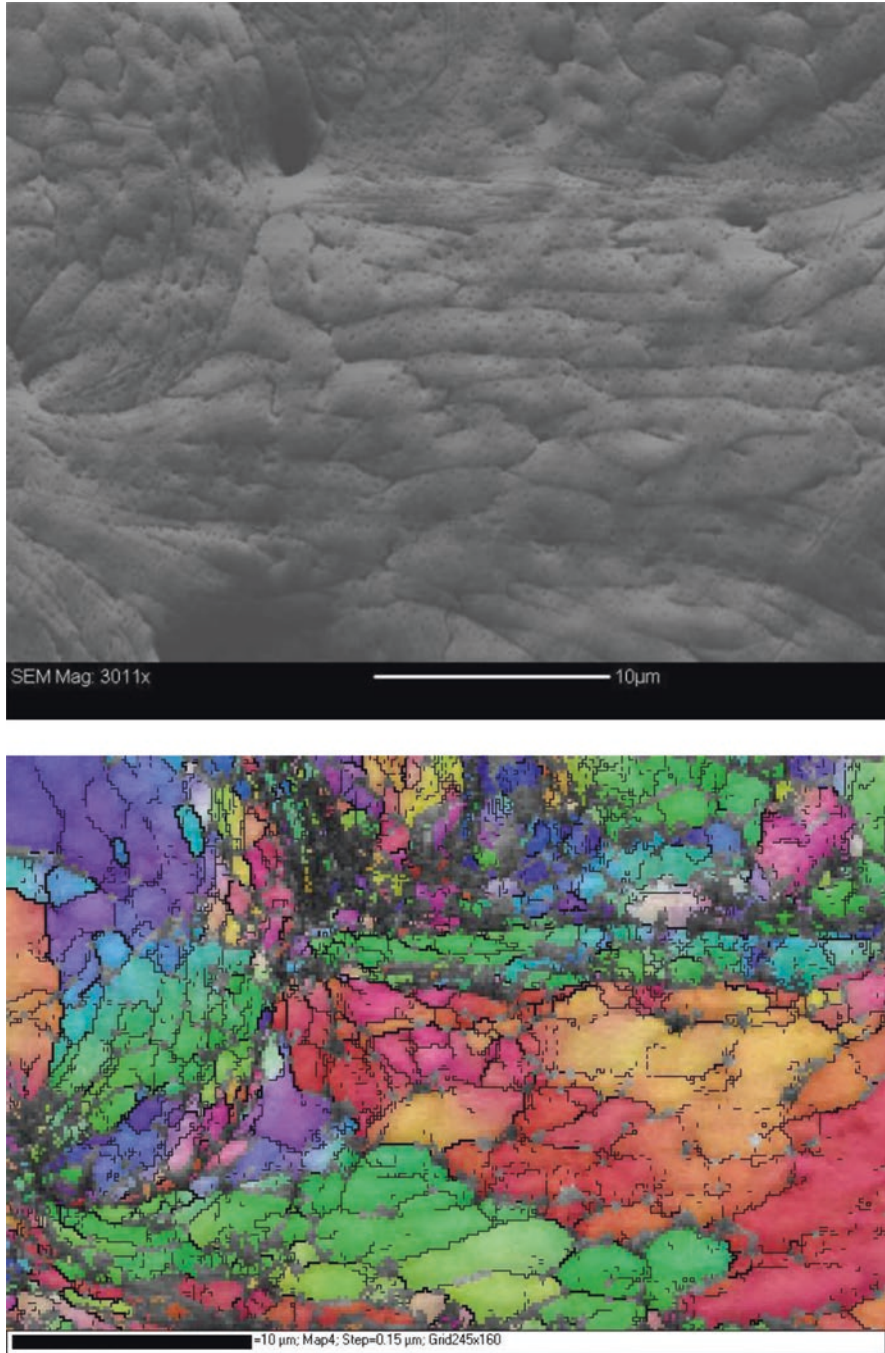


Fig. 16.17 (continued)

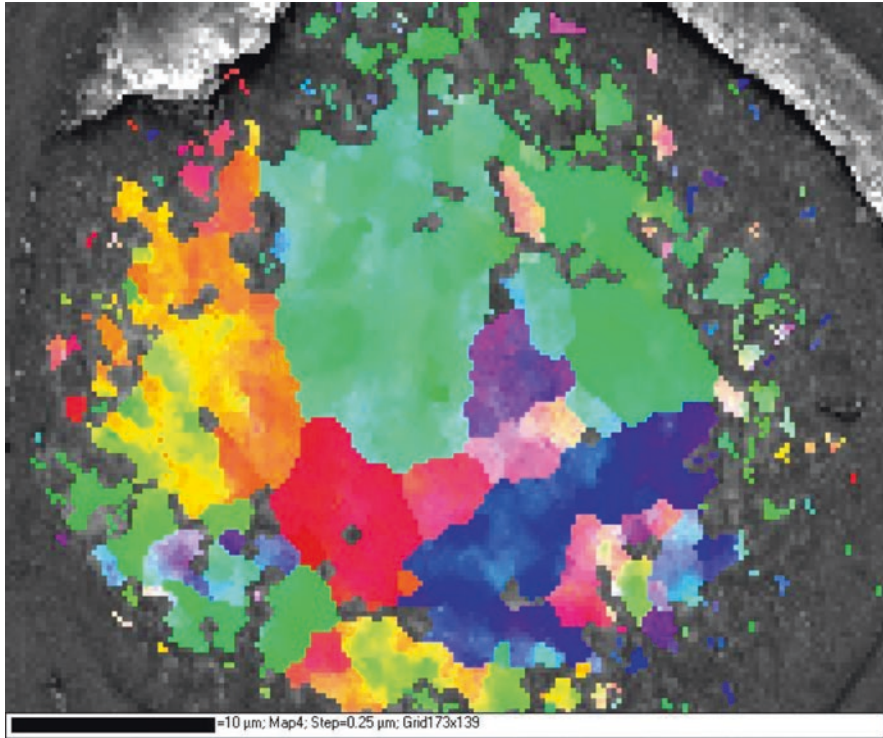


Fig. 16.17 (continued)

16.4.7 Modelling

Both the SPH and the Lagrangian models were able to reproduce the morphology of the deformed particle in a single particle simulation (Fig. 16.18) (Saleh et al. 2014a). This was also observed in earlier studies by (Schmidt et al. 2009; Gu and Kamnis 2009; Grujicic et al. 2004; Assadi et al. 2003). The simulations show that upon impact there is a narrow band at the periphery of the deposited cold spray particles where the temperature increases, and there is strong correlation with the adiabatic shear instability since these regions are characterized by a rapid decrease of the flow stress and a correspondingly rapid rise in plastic strain, as seen in Fig. 16.19. These regions are areas where material jetting is most pronounced and occurs at an angle of 40–45°, measured from the direction of the particle impact (Fig. 16.20). In these regions temperature can approach or exceed the melting point (Fig. 16.19) and therefore create conditions for efficient metallurgical bonding. The localization of both the temperature rise and the large plastic strains in the narrow region around the particle edge also supports the experimental observation of dynamic recrystallization as seen in the EBSD image in Fig. 16.17, with the associated grain refinement in the areas adjacent to the contact boundary.

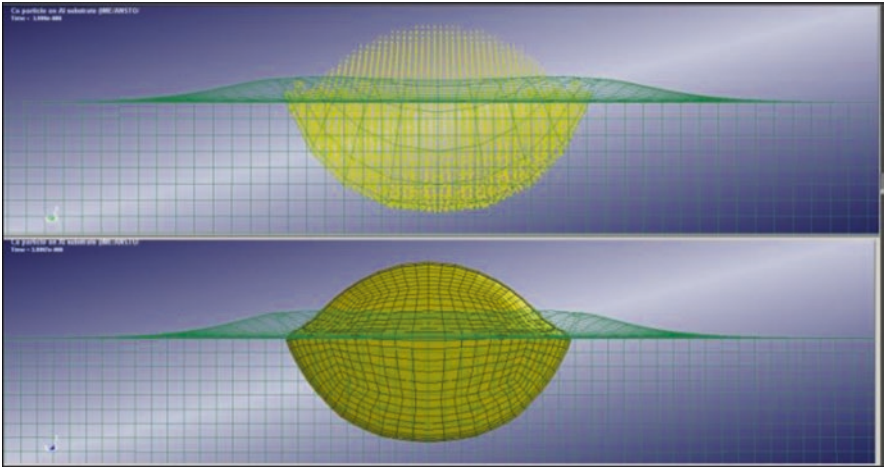


Fig. 16.18 A single particle shape simulation: particle shape by (a) SPH and (b) Lagrangian methods

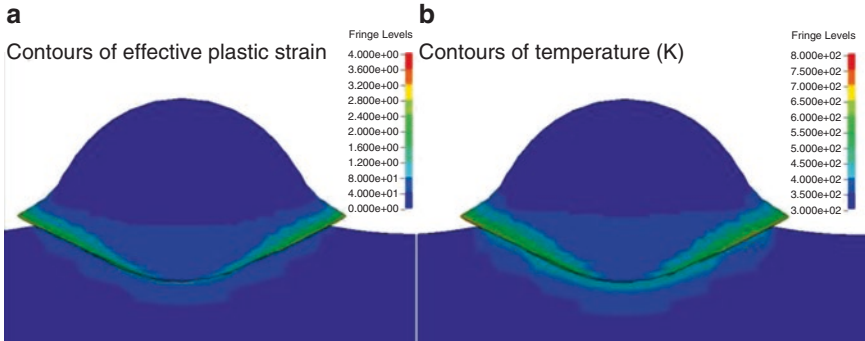


Fig. 16.19 LE single particle shape simulation: localization of (a) the effective plastic strain and (b) temperature. Original particle size is 15 μm

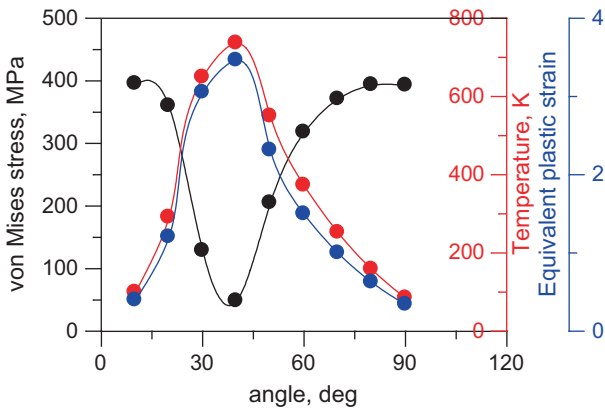


Fig. 16.20 Angular dependence of the localized peak effective plastic strain, stress flow and temperature along the particle contact boundary (in the LE single particle simulation)

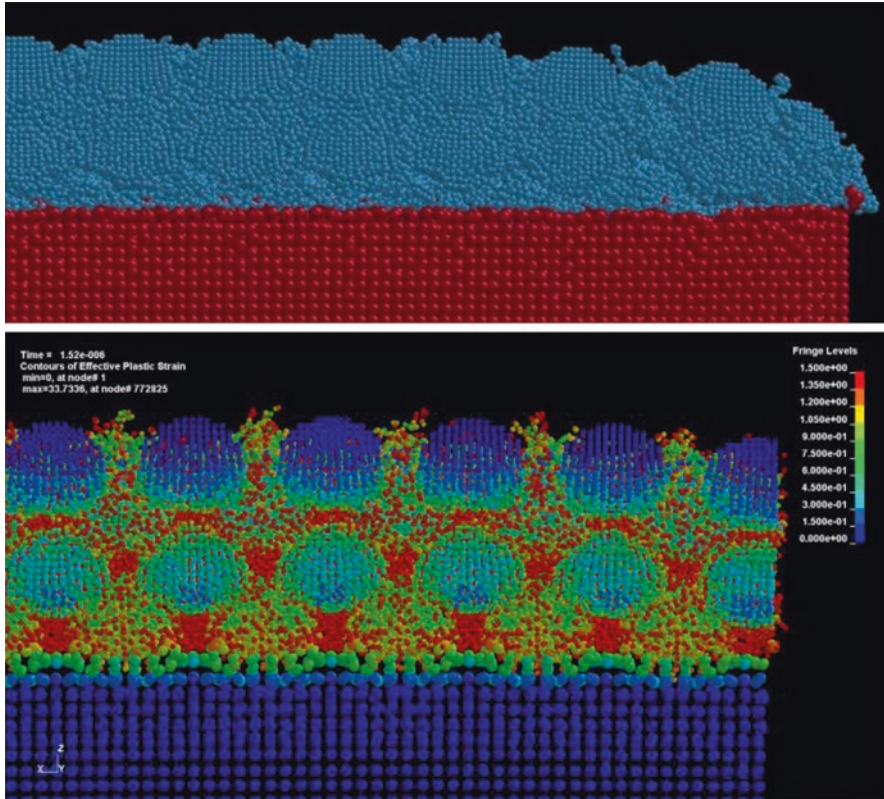


Fig. 16.21 Multiparticle SPH simulation: (a) multilayer morphology and (b) effective plastic strain map in the cross-section

The results of the multiparticle SPH simulations show the morphology of the cold spray particles is unequivocally affected by the impact of the particle and also by impacts of the particles impacting surface thereafter (Fig. 16.21). The jetting of materials from neighbouring particles allows for lateral linkages through mechanical locking of the semi-molten metals as they cool, but perhaps the more significant effect is the metallurgical bonding in the contact area between particles in the molten conditions. The SPH model was also able to predict two aspects of the stress accumulation during spraying. First, the large compressive stresses induced by the sprayed particles in the substrate due to the shot peening effects. Second, for the coating the model produces an average compressive deposition stress of approximately -10 MPa, which is consistent with the measured value for pure Al in Fig. 16.16 (-17 ± 7 MPa for KM and -8 ± 2 for

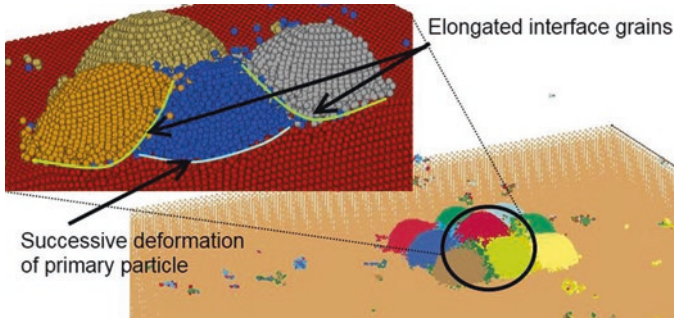


Fig. 16.22 Some details of multiparticle interaction: particle interfaces, ejected material

CGT), but somewhat smaller than for the Al6061 alloy sprayed by KM (-35 ± 6 MPa) (Spencer et al. 2012).

The limited number of particle that can be practically modelled may be responsible since the surface stress relaxation effect is still significant for such a limited thickness of the coating. Another drawback of the model was the almost instantaneous (adiabatic) deposition of all particles rather than the staggered deposition that would allow some heat dissipation, conduction and diffusion; it can be improved in future simulations. Therefore, if these effects are taken into account, this should result in larger compressive stresses. Another result of multiparticle simulation is that model predicts some jetting with material escaping the surface (Fig. 16.22). This results in deposition efficiency less than 100%. There is also some porosity as result of particle-particle collisions and the initially staggered formation, with a resultant computed density being less than bulk. Overall, the reproduction of the particle shape after impact, material jetting and the residual stress profile all suggest that the SPH model can be used to describe multiple particle deposition in cold spray coatings.

16.5 Summary and Conclusions

1. Spraying using CGT, with a higher temperature and velocity, produces coatings with slightly better mechanical properties (Young's modulus, density), owing to the higher compaction and a reduction in the bulk and interfacial defects.
2. Texture analysis using neutron diffraction demonstrates very weak preferred orientation development, suggesting very limited role of deformation by dislocation glide modes. These results suggest that the core of individual particles may not substantially deform and other deformation mechanisms that do not cause lattice rotation are potentially involved, e.g. adiabatic shear banding assisted by local annealing. This is

supported by the EBSD analysis with evidence of the dynamic recrystallization in the particle interface regions as well as the results of simulation.

3. Results of modelling a single particle collision event show that the local temperature may exceed the melting point in the narrow band along particle interfaces. The multiple particle deposition simulation suggests very localized deformation and cohesion with formation of splat-to-splat contacts.
4. The compressive residual stress due to peening effects was confirmed, though for many materials, it is very close to zero. The magnitude of the peening stress is intimately linked to the material's plastic properties. Strong residual stress accumulation is more typical for FCC materials, with their ability to plastically deform and their propensity to form a better splat-to-splat contact. This enables the accumulation of residual stresses whose magnitude, if not proportional, then at least correlates with the yield stress of the materials.
5. The magnitude of the peening stress can also be predicted by the SPH method with multiple particle impact simulation and performing macroscopic averaging over large ensemble of the deposited particles resulting into compressive (peening) overall stress. A significant progress has been achieved in this direction: for the first time, the multiple particle simulation of CS process has been performed using the SPH formulation on a system of 400 individual particles and encompassed more than 1 million individual SPH elements with quantitative metrics used to validate the model's outputs. Experimentally observed peening stress is also predicted by the SPH method and used to validate the model.
6. The detailed 3D maps of the plastic strain and elastic strain fields available through the multiple particle simulation accentuate the highly non-uniform nature of the material on the microscopic level that is underscored by the EBSD analysis. Linking these different scales of physics of the cold spray process is a difficult and problematic task. Relative success can be achieved using empirical modelling approach, when an analytical relationship can be drawn for the residual stress as a function of the yield stress (Spencer et al. 2012; Luzin et al. 2011).
7. Regarding the particle bonding mechanism, our study (experimental and modelling) offers a more or less comprehensive view of the CS process: despite the term "cold", the CS is, in fact, very thermal in nature with splat-to-splat bonding better characterized as a "micro-welding"; when in the very narrow peripheral contact areas of a particle temperatures exceed the melting points, the material is hugely deformed in its plastically soft condition and recrystallized. Therefore, "micro-welding" provides metallurgical bonding, while mechanical interlocking seems to be less important, though it can have a place through jetting. In contrast to the outer periphery of a particle, the central core remains largely undeformed as supported by the weak texture measurements. Deformation in the transitional zone and the formation of preferred orientation are more apparent in the particle-substrate and particle-particle interfaces.
8. Finally, for the empirical studies of the mechanism of coating formation in cold spray, the neutron diffraction stress scanning technique is very useful, while the use of other material characterization techniques greatly extends the degree of understanding of the process.

References

- Assadi H, Gärtner F, Stoltenhoff T, Kreye H (2003) Bonding mechanism in cold gas spraying. *Acta Mater* 51(15):4379–4394
- Brenner A, Senderoff S (1949) Calculation of stress in electrodeposits from the curvature of a plated strip. *J Res Natl Bur Stand* 42:105–123
- Cho J-H, Rollett AD, Oh KH (2004) Determination of volume fractions of texture components with standard distributions in Euler space. *Metall Mater Trans A* 35(13):1075–1086
- Choi WB, Li L, Luzin V, Neiser R, Gnäupel-Herold T, Prask HJ, Sampath S, Gouldstone A (2007) Integrated characterization of cold sprayed aluminum coatings. *Acta Mater* 55(3):857–866
- Dykhuizen RC, Smith MF (1998) Gas dynamic principles of cold spray. *J Therm Spray Technol* 7(2):205–212
- Genzel CH (2004) Diffraction stress analysis in thin films and coatings – problems, methods and perspectives. *J Neutr Res* 12:233–241
- Grujicic M, Zhao CL, DeRosset WS, Helfritsch D (2004) Adiabatic shear instability based mechanism for particles/substrate bonding in the cold-gas dynamic-spray process. *Mater Des* 25(8):681–688
- Gu S, Kamnis S (2009) Bonding mechanism from the impact of thermally sprayed solid particles. *Metall Mater Trans A* 40(11):2664–2674
- Heritage K, Frisby C, Wolfenden A (1988) Impulse excitation technique for dynamic flexural measurements at moderate temperature. *Rev Sci Instrum* 59(6):973–974
- Hutchings MT, Krawitz AD (eds) (1992) *Measurement of residual and applied stress using neutron diffraction*. NATO science series E 216. Springer, Netherlands
- Hutchings MT, Withers PJ, Holden TM, Lorentzen T (2005) *Introduction to the characterization of residual stress by neutron diffraction*. Taylor & Francis Ltd, Boca Raton
- Kirstein O, Luzin V, Garbe U (2009) The strain-scanning diffractometer Kowari. *Neutron News* 20(4):34–36
- Korsunsky AM (2005) The modelling of residual stresses due to surface peening using eigenstrain distributions. *J Strain Anal Eng* 40(8):817–824
- Luzin V, Valarezo A, Sampath S (2008) Through-thickness residual stress measurement in metal and ceramic spray coatings by neutron diffraction. *Mater Sci Forum* 571-572:315–320
- Luzin V, Matějček J, Gnäupel-Herold T (2010) Through-thickness residual stress measurement by neutron diffraction in Cu+W plasma spray coatings. *Mater Sci Forum* 652:50–56
- Luzin V, Spencer K, Zhang MX (2011) Residual stress and thermo-mechanical properties of cold spray metal coatings. *Acta Mater* 59(3):1259–1270
- Luzin V, Vackel A, Valarezo A, Sampath S (2017) Neutron through-thickness stress measurements in coatings with high spatial resolution. *Mater Sci Forum*, in press
- Matejček J, Sampath S, Brand PC, Prask HJ (1997) Residual stress measurement on thermally sprayed coatings. In: *Proceedings of the 15th international thermal spray conference*, Indianapolis, USA, pp 861–866
- Matejček J, Sampath S, Brand PC, Prask HJ (1999) Quenching, thermal and residual stress in plasma sprayed deposits: NiCrAlY and YSZ coatings. *Acta Mater* 42(7):607–617
- Matejček J, Sampath S (2003) In situ measurement of residual stresses and elastic moduli in thermal sprayed coatings: part 1: apparatus and analysis. *Acta Mater* 51(3):863–872
- Matthies S, Vinel GW, Helming K (1987) *Standard distributions in texture analysis: maps for the case of cubic-orthorhombic symmetry*. Akademie-Verlag, Berlin
- Papyrin PA, Kosarev PV, Klinkov DS, Alkimov PA, Fomin PV (2007) *Cold spray technology*. Elsevier, Oxford
- Pirling T (2011) Precise analysis of near surface neutron strain imaging measurements. *Procedia Eng* 10:2147–2152
- Saleh M, Luzin V, Spencer K (2014a) Analysis of the residual stress and bonding mechanism in the cold spray technique using experimental and numerical methods. *Surf Coat Technol* 252:15–28

- Saleh M, Luzin V, Spencer K (2014b) Evaluation of the residual stress in the cold spray technique using smooth particle hydrodynamics modelling and neutron diffraction. *Mater Sci Forum* 777:205–212
- Santana YY, Renault PO, Sebastiani M, La Barbera JG, Lesage J, Bemporad E, Le Bourhis E, Puchi-Cabrera ES, Staia MH (2008) Characterization and residual stresses of WC-co thermally sprayed coatings. *Surf Coat Technol* 202:4560–4565
- Schmidt T, Assadi H, Gärtner F, Richter H, Stoltenhoff T, Kreye H, Klassen T (2009) From particle acceleration to impact and bonding in cold spraying. *J Therm Spray Technol* 18(5):794–808
- Spencer K, Luzin V, Matthews N, Zhang MX (2012) Residual stresses in cold spray Al coatings: the effect of alloying and of process parameters. *Surf Coat Technol* 206(19–20):4249–4255
- Stoney GG (1909) The tension of Metallic films deposited by electrolysis. *Proc Roy Soc Lond A* 82:172–175
- Suzuki H, Harjo S, Abe J, Xu P, Aizawa P, Akita K (2013) Effects of gauge volume on pseudo-strain induced in strain measurement using time-of-flight neutron diffraction. *Nucl Instrum Meth A* 715:28–38
- Tsui YC, Clyne TW (1997a) An analytical model for predicting residual stresses in progressively deposited coatings part 1: planar geometry. *Thin Solid Films* 306(1):23–33
- Tsui YC, Clyne TW (1997b) An analytical model for predicting residual stresses in progressively deposited coatings part 1: cylindrical geometry. *Thin Solid Films* 306(1):34–51
- Twiss R (1997) Theory and applicability of a recrystallized grain size paleopiezometer. *Pageoph* 115(1–2):227–244
- Zou Y, Qin W, Irissou E, Legoux J-G, Yue S, Szpunar JA (2009) Dynamic recrystallization in the particle/particle interfacial region of cold-sprayed nickel coating: electron backscatter diffraction characterization. *Scripta Mater* 61(9):899–902